Biosensors and Bioelectronics 145 (2019) 111638

Contents lists available at ScienceDirect

Biosensors and Bioelectronics

journal homepage: www.elsevier.com/locate/bios

Simple one-pot aqueous synthesis of 3D superstructured PtCoCuPd alloyed tripods with hierarchical branches for ultrasensitive immunoassay of cardiac troponin I

Yao Chen[a], Li-Ping Mei[a], Jiu-Ju Feng[a,**], Pei-Xin Yuan[a], Xiliang Luo[b], Ai-Jun Wang[a,*]

[a] Key Laboratory of the Ministry of Education for Advanced Catalysis Materials, College of Chemistry and Life Sciences, College of Geography and Environmental Sciences, Zhejiang Normal University, Jinhua, 321004, China

[b] Key Laboratory of Sensor Analysis of Tumor Marker, Ministry of Education, College of Chemistry and Molecular Engineering, Qingdao University of Science and Technology, Qingdao, 266042, China

ARTICLE INFO

Keywords:
One-pot aqueous method
Electrochemical immunosensor
Tripods
Hierarchical branches
Cardiac troponin I

ABSTRACT

By integrating the amplified electrochemical signals and effective capture of antibodies together, advanced multimetallic superstructured nanocrystals endow label-free immunosensors promising applications in early diagnosis and monitoring of diseases. Herein, four-metallic PtCoCuPd hierarchical branch-like tripods (HBTPs) were directly synthesized by a green one-pot aqueous method without any seed or organic solvent involved, which were applied to construct a novel label-free immunosensor for detecting cardiac troponin I (cTnI). The specific hierarchical micro/nanostructures greatly improved the immobilization of antibodies and enhanced the catalytic activity for $K_3Fe(CN)_6$, which would effectively amplify the electrochemical signals, thereby improving the detection sensitivity. Under the optimal conditions, the as-developed immunosensor exhibited a wide linear range (0.001–100.0 ng mL^{-1}) and a low detection limit (0.2 pg mL^{-1}, $S/N = 3$) for the assay of cTnI. The immunosensor provides a powerful platform for quantitative detection of cTnI, which can be explored to detect other tumor markers in actual sample analysis.

1. Introduction

Acute myocardial infarction (AMI) is one of the most common causes of death, which seriously threatens human health (Spain et al., 2018). Cardiac troponin I (cTnI) is considered as the primary marker of myocardial injury for AMI, owing to its excellent specificity and long detection window (Dhawan et al., 2018). The normal level of cTnI in human serum is less than 0.4 ng mL^{-1}, while the abnormal concentrations indicate an increased risk of getting AMI (Qian et al., 2019).

Conventionally, enzyme-linked immunoassay (ELISA) (Cho et al., 2009) and fluorescence analysis (Seo et al., 2016) are the most common methods to detect cTnI (Qian et al., 2019). Nevertheless, they are commonly time-consuming and laborious, usually involving expensive instruments. Therefore, it is of great significance to develop a sensitive and simple method for early accurate diagnosis of AMI (Liu et al., 2016; Ye et al., 2019; Zhou et al., 2017).

Generally, electrochemical analysis is the most commonly used in environmental monitoring and food analysis (Asif et al., 2018; Wen et al., 2017). It has the merits of high accuracy, wide measurement range, simple instrument and easy automation (Gao et al., 2017; Lv et al., 2019; Zhang et al., 2019). The electrochemical immunosensor, as a branch of electrochemical analysis, takes the advantage of highly specific immune recognition between antigens and antibodies to detect the analyte (Haji-Hashemi et al., 2018). It not only integrates the above advantages together, but also detects the target specifically and selectively (Zhang et al., 2019).

Compared with sandwich-type strategy, label-free electrochemical immunosensor with simple and quick operation has great promising applications in clinical diagnosis and monitoring of the diseases (Chen et al., 2019b; Yang et al., 2017). Amplifying the electrochemical signals and the effective capture of antibodies are the two bottlenecks to achieve high sensitivity and ultralow detection limit (*LOD*) for such immunosensors (Zhang et al., 2018).

Recently, rapid development of precious metal nanomaterials such as gold (Au) (Ma et al., 2017), platinum (Pt) (Yang et al., 2015) and palladium (Pd) (Qi et al., 2014) has wide applications in bioanalysis,

* Corresponding author.
** Corresponding author.
E-mail addresses: jjfeng@zjnu.cn (J.-J. Feng), ajwang@zjnu.cn (A.-J. Wang).

https://doi.org/10.1016/j.bios.2019.111638
Received 6 July 2019; Received in revised form 9 August 2019; Accepted 26 August 2019
Available online 29 August 2019
0956-5663/

thanks to their unprecedented catalytic activity, good biocompatibility and high electronic conductivity (Dai et al., 2019). Among them, noble metals doped with non-noble metals (e.g. Co, Cu, Mo and Ni) can dramatically reduce the preparation cost and enhance the catalytic properties via the synergistic effects of different metals (Liu et al., 2018; Yan et al., 2018). For example, trimetallic NiAuPt nanoparticles (NPs) exhibited superior electrocatalytic properties towards the reduction of H_2O_2 due to the incorporation of Ni, enabling ultrasensitive detection of carcinoembryonic antigen (CEA) (Tian et al., 2016). Another example is that Pd NPs doping wrinkled amorphous MoS_x (Pd NPs@MoS_x) provided a platform for insulin detection (Gao et al., 2019).

Apart from the composition influence, the morphology and structure of nanomaterials are also critical to improve the catalytic performances (Wang et al., 2019a; Zhu et al., 2015). Rhombic dodecahedral Cu_3Pt nanoframes with promoted oxygen reduction property achieved highly sensitive detection of alpha fetal protein (AFP) (Wang et al., 2019b). Sea-urchin-like PdAuCu nanocrystals (NCs) largely amplified the electrochemical responses, enabling the sensitive analysis of CEA (Chen et al., 2019a). The unique hollow dendritic AuPtAg NCs displayed the steeply enlarged surface area, showing the very good analytical performance for prostate specific antigen (PSA) detection (Shi et al., 2018).

Herein, multimetallic PtCoCuPd HBTPs were directly synthesized with the aid of F127 by a green one-pot aqueous method without any seed or organic solvent. A PtCoCuPd HBTPs-based label-free immunosensor was fabricated by virtue of the catalytic signals of $K_3Fe(CN)_6$ to electrochemically detect cTnI (see Fig. 1). Furthermore, the as-developed immunosensor is further implemented for the assay of cTnI in actual serum sample.

2. Experimental

2.1. Synthesis of PtCoCuPd HBTPs

Briefly, the mixture of H_2PtCl_6 (3 mmol L^{-1}, 0.78 mL), $C_4H_6CoO_4$ (3 mmol L^{-1}, 1.5 mL), $CuCl_2{\cdot}2H_2O$ (3 mmol L^{-1}, 1.5 mL), Na_2PdCl_4 (7.5 mmol L^{-1}, 0.75 mL), HCl solution (0.18 mol L^{-1}, 0.15 mL), KBr (300 mg) and Pluronic F127 (75 mg) was ultrasonicated for 30 min to form a homogeneous suspension. Immediately, l-ascorbic acid (AA) solution (0.1 mol L^{-1}, 3 mL) was put into the mixture, the reaction system was heated up to 95 °C and then reacted for 3 h in oil bath. The resulting PtCoCuPd HBTPs were centrifuged at 7000 rpm and washed several times with water and dried at 60 °C for further use.

For comparison, PtCoPd NPs and PtPd NPs were synthesized consistently with the H_2PtCl_6 (3 mmol L^{-1}, 0.78 mL) + $C_4H_6CoO_4$ (3 mmol L^{-1}, 1.5 mL) + Na_2PdCl_4 (7.5 mmol L^{-1}, 0.75 mL) and H_2PtCl_6 (3 mmol L^{-1}, 0.78 mL) + Na_2PdCl_4 (7.5 mmol L^{-1}, 0.75 mL) as the metal precursors, respectively, while the other operational conditions were remained the same.

2.2. Construction of PtCoCuPd HBTPs-based immunosensor

Briefly, a glassy carbon electrode (GCE, 3 mm in diameter) was carefully polished with Al_2O_3 powder (0.5 μm). Firstly, the uniform dispersion of the as-constructed PtCoCuPd HBTPs (1.5 mg mL^{-1}, 6 μL) was instantly covered onto the electrode surface and dried at room temperature, defined as PtCoCuPd HBTPs/GCE for clarity. Then, the cardiac troponin I antibody (Ab) solution (20 μg mL^{-1}, 6 μL) was effectively immobilized onto the modified electrode and dried at 4 °C overnight (denoted as Ab/PtCoCuPd HBTPs/GCE), by virtue of the highly specific interactions between the amino group of the antibody and Pt (Wu et al., 2013). Next, bovine serum albumin (BSA) solution (1 *wt*%, 5 μL) was coated at 37 °C for 1 h to eliminate non-specific adsorption sites, defined as BSA/Ab/PtCoCuPd HBTPs/GCE. After that, the BSA/Ab/PtCoCuPd HBTPs/GCE was immersed into the cTnI antigen (Ag) solution with different concentrations (0.001-100.0 ng mL^{-1}) at 37 °C for 1 h, followed by storing at 4 °C prior to use. It was worth noting that the physical adsorption was efficiently eliminated by slightly washing with phosphate buffered solution (PBS, 0.1 mol L^{-1}, pH 7.4) after each step. In this protocol, the cTnI immunosensor was developed by using $K_3[Fe(CN)_6]$ as the signal probe (as depicted in Fig. 1).

More information about the *Materials and chemicals*, *Apparatus* and *Electrochemical measurements* were provided in Supporting Information (SI).

3. Results and discussion

3.1. Characterization of PtCoCuPd HBTPs

The structural features of PtCoCuPd HBTPs were seriously characterized by scanning electron microscopy (SEM) and transmission electron microscopy (TEM). As observed in Fig. 2A–D, plenty of well-

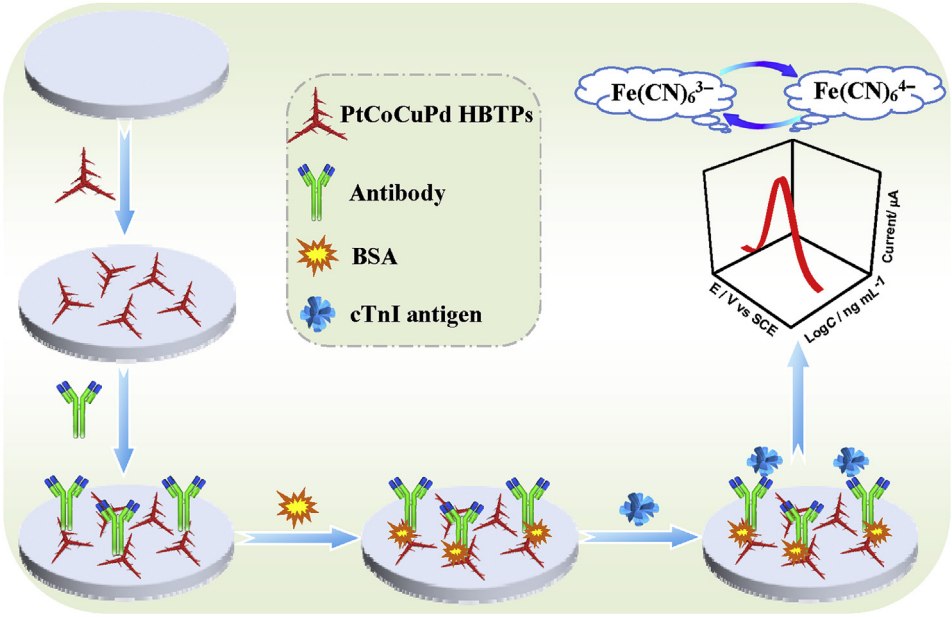

Fig. 1. Schematic illustration of the PtCoCuPd HBTPs-based electrochemical immunosensor for detecting cTnI.

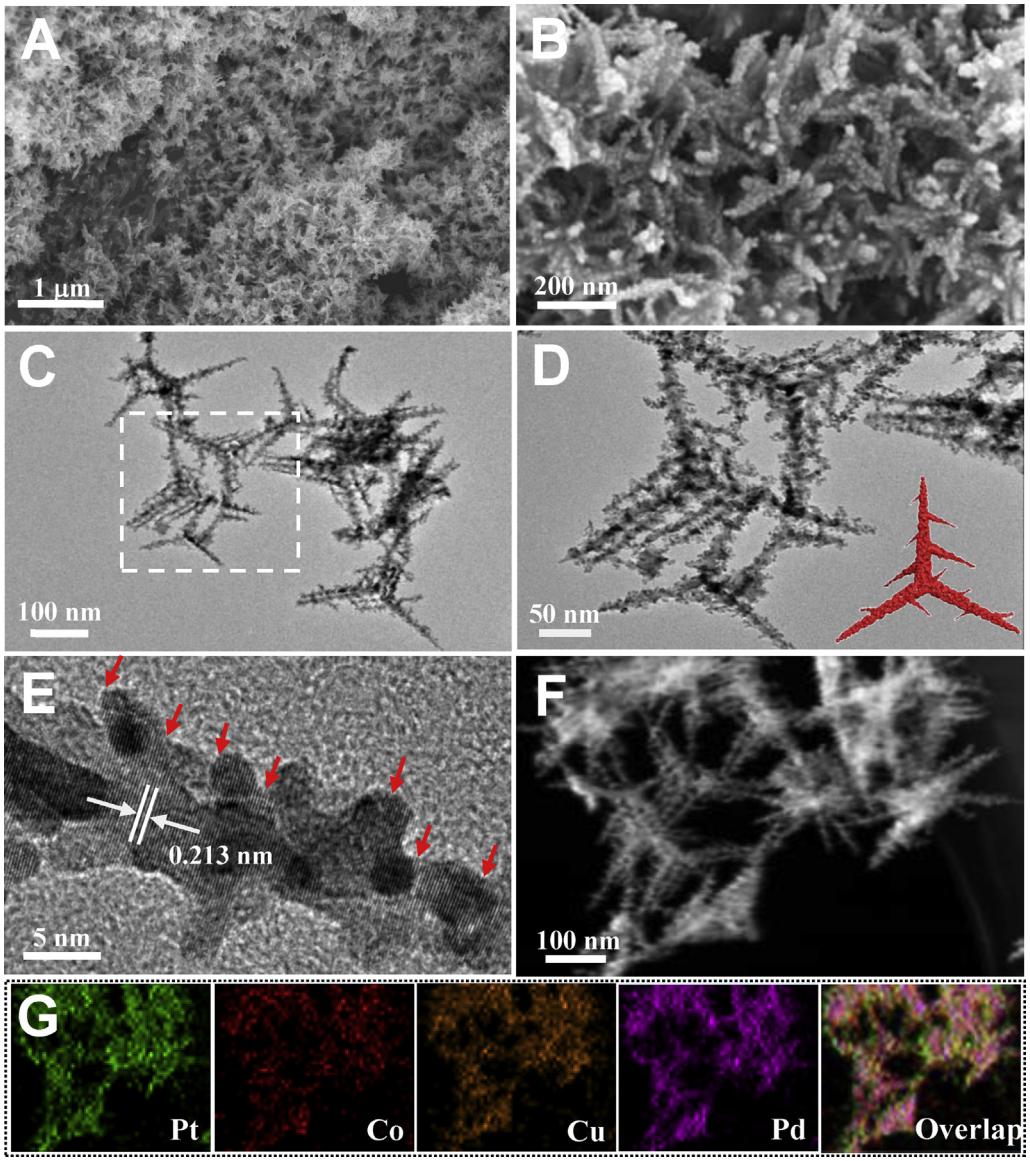

Fig. 2. (A–B) SEM images of PtCoCuPd HBTPs. (C–D) Low- and (E) high-magnification TEM images. (F–G) HAADF-STEM-EDS mappings. Inset in D shows the 3D geometric model.

defined hierarchical branch-like configurations show up with uniform size. Furthermore, each particle exhibits typically tripod-like structures, along with the wide angle of the adjacent branches with the value of about 120°. The average length and width of each branch are approximately 93.28 nm and 7.86 nm, respectively. Among them, each branch has an outer protruding small edge with rough surface and the length of about 8.26 nm. As revealed by the high-resolution TEM (HRTEM) image (Fig. 2E), there appear clear lattice fringes with the neighboring lattice spacing distance of 0.213 nm. Meanwhile, the atomic steps above the branched exteriors are clearly observed, as shown by the red arrows, which would promote the catalytic activity (Wang et al., 2018).

The structure and elemental distribution are strongly certificated via high-angle annular dark-field scanning transmission electron microscopy-energy dispersive X-ray spectroscopy (HAADF-STEM-EDS, Fig. 2F and G). From the mapping images, Pt, Co, Cu and Pd elements are evenly distributed throughout the whole typical sample, demonstrating the alloy character (Wang et al., 2018). Additionally, the atomic ratio of Pt, Co, Cu and Pd is estimated to be 18.89: 60.89: 0.65: 19.57 by the EDS analysis, which agrees well with the analysis of the line scanning curves (Fig. 3A and B).

X-ray diffraction (XRD) pattern of PtCoCuPd HBTPs exhibits five distinct diffraction peaks at 40.3°, 46.8°, 68.7°, 82.8° and 87.2°, associated with the (111), (200), (220), (311) and (222) crystal planes of the representative *fcc* metallic structure, respectively (Fig. 3C). Notably, no diffraction peaks of pure Pt, Co, Cu and Pd show up, indicating the well-alloyed nature of PtCoCuPd HBTPs (Wang et al., 2018). Meanwhile, these diffraction peaks are slightly shifted to the higher angle with respect to standard patterns of pure Pt and Pd, due to the alloy nature of Pt, Co, Cu and Pd (Wang et al., 2018).

X-ray photoelectron spectroscopy (XPS) characterization can further illuminate the surface compositions and valence states of advanced materials (Wang et al., 2018). Obviously, there are Pt, Co, Cu, Pd and O elements detected in the survey XPS spectrum of the PtCoCuPd HBTPs (Fig. 3D). In the high-resolution XPS segment of Pt 4f (Fig. 4A), the stronger couple for $4f_{7/2}$ (70.9 eV) and $4f_{5/2}$ (74.3 eV) is the characteristics of metallic Pt^0, while the weaker pair for $4f_{7/2}$ (71.8 eV) and $4f_{5/2}$ (75.2 eV) is attributed to Pt^{2+} species, suggesting the predominant Pt^0 in the product.

For the high-resolution Pd 3d segment (Fig. 4B), the two strong

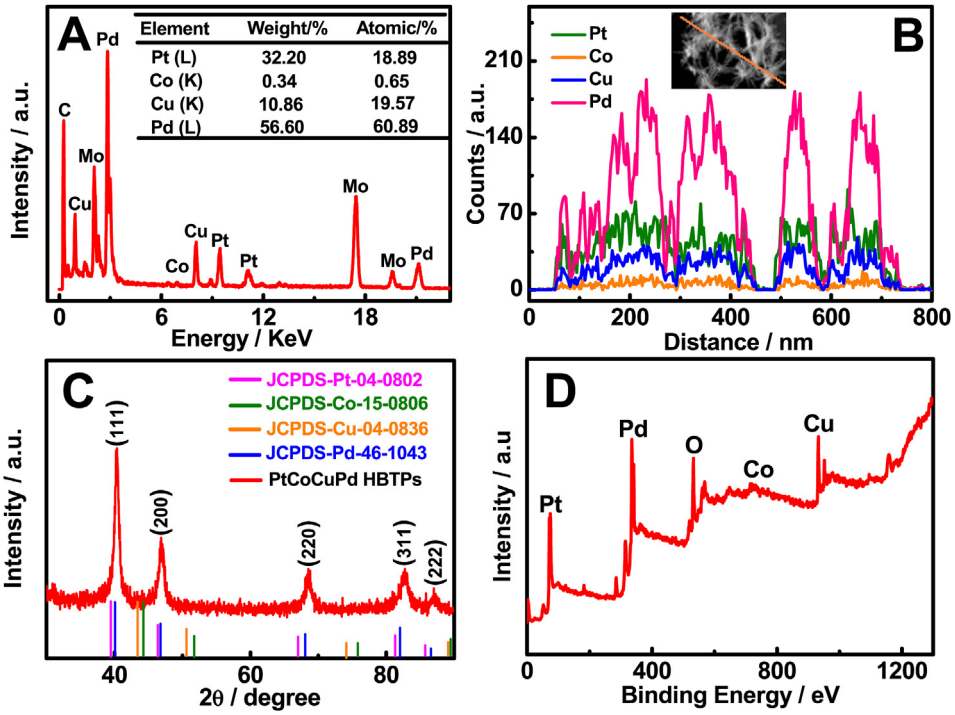

Fig. 3. (A) EDS spectrum, (B) line scanning profiles, (C) XRD pattern, and (D) survey XPS spectrum of PtCoCuPd HBTPs. Standard XRD spectra of pure Pt (JCPDS 04–0802), Co (JCPDS 15–08036), Cu (JCPDS 04–0836) and Pd (JCPDS 46–1043) were provided for comparison. Inset in B shows the HAADF-STEM image.

peaks are deconvoluted into four peaks, which indicate the coexistence of Pd^0 and Pd^{2+}. Moreover, there are no obvious peaks observed in the high-resolution Co 2p region (Fig. 4C), owing to the very limited content of Co. These phenomena coincide well with the EDS analysis. In addition, the peak area of Cu^0 far exceeds that of Cu^{2+} in this research, manifesting the efficient reduction of the Cu precursor in this synthesis (Fig. 4D).

Taken together, the formation mechanism of the PtCoCuPd HBTPs is described briefly. At the very initial stage, the four metal precursors ($PtCl_6^{2-}$, Co^{2+}, Cu^{2+} and $PdCl_4^{2-}$) are simultaneously reduced to Pt, Co, Cu and Pd atoms in the existence of AA. When the concentrations of the newly-generated atoms reachsaturation, they quickly gather together to yield well-dispersed PtCoCuPd nuclei via homogeneous nucleation (Shao et al., 2016). Meanwhile, the as-formed PtCoCuPd nuclei

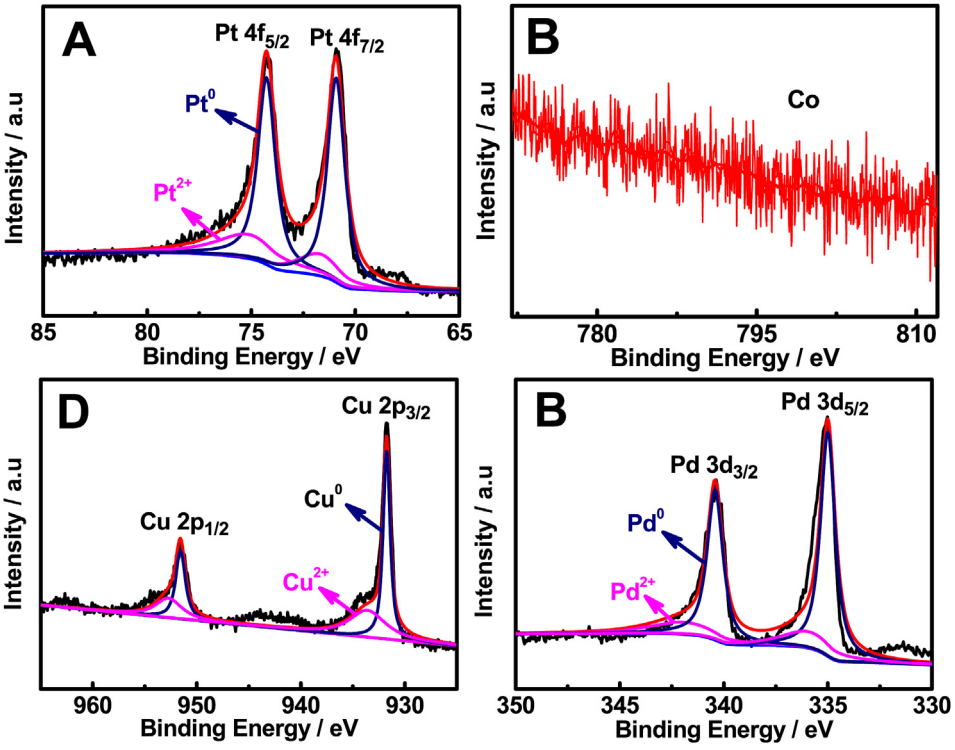

Fig. 4. High-resolution (A) Pt 4f, (B) Co 2p, (C) Cu 2p and (D) Pd 3d XPS spectra of PtCoCuPd HBTPs.

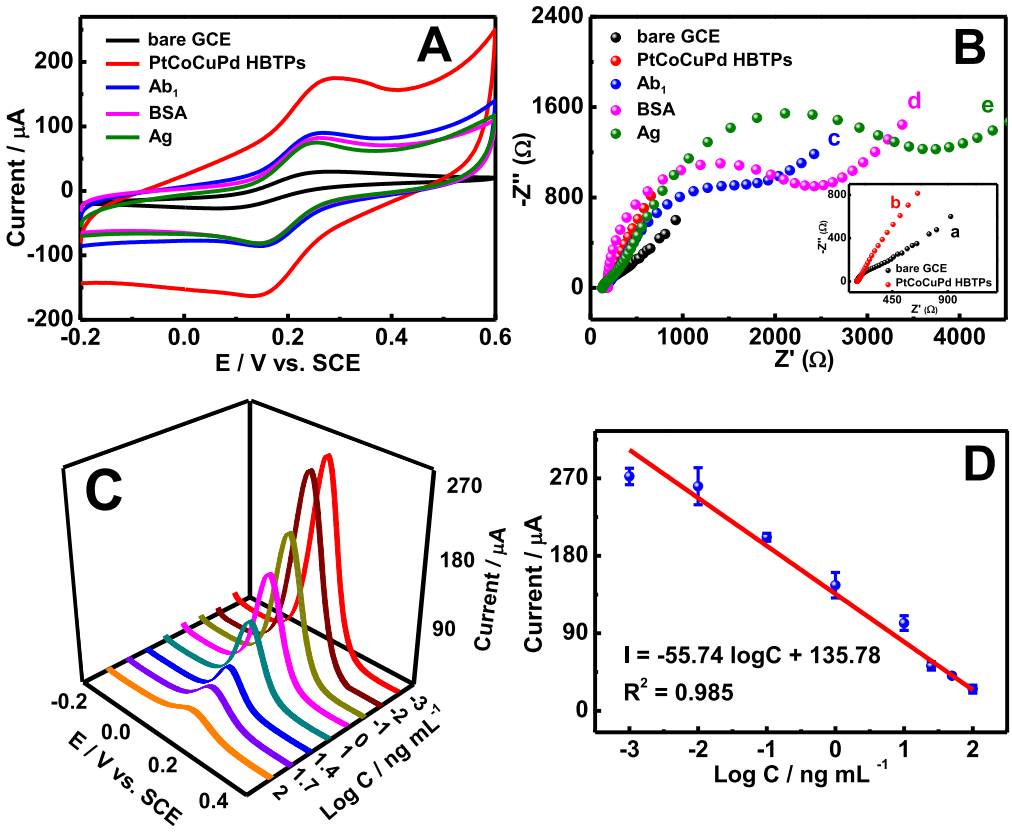

Fig. 5. (A) CV plots and (B) EIS of the fabricated immunosensor in 0.1 moL L^{-1} KCl solution containing 2.5 mmol L^{-1} $Fe(CN)_6^{3-/4-}$. (C) DPV plots in the presence of 0.001, 0.01, 0.1, 1.0, 10.0, 25.0, 50.0 and 100.0 ng mL^{-1} cTnI. (D) The calibration plot (Error bar = *SD*, n = 5).

undergo rapid and full coverage with the adjacent F127 molecules to improve the dispersion and simultaneously minimize the surface free energy (Shao et al., 2017). Ultimately, the typical PtCoCuPd HBTPs are produced via nucleation, epitaxial-growth and Ostwald ripening. In this synthesis, F127 plays a decisive role in the branching growth of the hierarchical PtCoCuPd architectures as a growth-directing agent (Wang et al., 2018).

3.2. Electrochemical characterization of the immunosensor

Cyclic voltammetry (CV) and electrochemical impedance spectroscopy are commonly adopted to carefully monitor the electrode interface characteristics of the immunosensor via stepwise assembly (Dai et al., 2019). Fig. 5A provides the CV plots of the PtCoCuPd HBTPs-based immunosensors. There appears a weak peak current on bare GCE (curve a). After efficient modification with PtCoCuPd HBTPs, the peak current increases sharply (curve b), which is six times enlargement relative to that of bare electrode. This is attributed to the unique PtCoCuPd HBTPs with abundant branched exteriors, enriched accessible active sites and synergistic effects of the four metals (Wang et al., 2018). Obviously, the current adversely decreases by further linkage of Ab onto the electrode (curve c), reflecting severe impediment of the electron transfer process and the efficient assembly (Chen et al., 2019a). With the subsequent immobilization of BSA (curve d) and cTnI (curve e), the redox peak currents show gradually declined trend, indicating that the deposited immune complexes occupy the electron transfer channels between the probe and electrode interface (Lv et al., 2019). This means the effective capture of the biomacromolecules on the electrode surface (Wang et al., 2019b).

Electrochemical impedance spectrum (EIS) usually consists of two parts: a linear diffusion region at the lower frequencies and a semicircular mass transfer resistance region at the higher frequencies, wherein the semicircular diameter is equivalent to the electron-transfer resistance (R_{et}) (Chen et al., 2019a). As displayed in Fig. 5B, the R_{et} of PtCoCuPd HBTPs/GCE (curve b) displays a straight line compared with that of bare GCE (curve a), indicating the competitive conductivity of PtCoCuPd HBTPs (Lv et al., 2019). More notably, the interfacial R_{et} values clearly increase with the stepwise modification of the electrode interfaces by Ab (curve c), BSA (curve d) and cTnI (curve e). These scenarios are explained by the fact that the immobilized proteins seriously inhibit the electron transport of the signal probe with the electrode. In the end, the CV and EIS data certificate the efficient assembly of the immunosensor (Shi et al., 2018).

3.3. The catalytic properties of PtCoCuPd HBTPs

It is well known that advanced nanomaterials with highly catalytic efficiency can significantly amplify the electrochemical signals and improve the analytical performance of immunosensor (Yang et al., 2017). Therefore, the acquisition of advanced nanomaterials with integrated advantages is the focus in recent researches (Mao et al., 2019). In this study, PtCoCuPd HBTPs serve as a feasible electrode material to steeply enhance the catalytic oxidation peak currents of K_3 [$Fe(CN)_6$], where homemade PtPd NPs and PtCoPd NPs behaved as the references.

Fig. S1A (SI) shows the differential pulse voltammetry (DPV) responses acquired in the PBS (0.1 moL L^{-1}, pH 7.4) containing 5.0 mmol L^{-1} K_3 [$Fe(CN)_6$]. Clearly, the PtCoCuPd HBTPs exhibit the sharply elevated peak current for oxidation of K_4 [$Fe(CN)_6$] to K_3 [$Fe(CN)_6$] (I = 226 μA), which is approximately 3- and 6-time enhancement alternative to those of PtCoPd NPs (I = 75 μA) and PtPd NPs (I = 38 μA) under the same experimental conditions. The merits are mainly attributed to the two aspects:(i) Synergistic effects of the four metals can dramatically accelerate the electron transfer rate and improve the stability with respective to the mono-, bi- and tri-metallic NPs

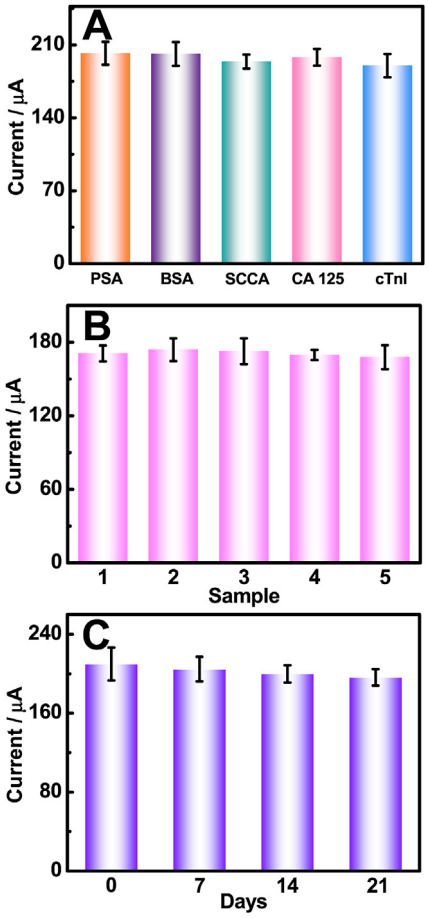

Fig. 6. (A) The currents towards 0.1 ng mL^{-1} cTnI without and with 100.0 ng mL^{-1} PSA, BSA, SCCA and CA125. (B) Electrochemical responses of the five immunosensor fabricated independently and (C) storage stability at 0.1 ng mL^{-1} cTnI (Error bar = *SD*, n = 5).

(Zhang et al., 2019). (ii) The distinctively spatial branch-like architectures can provide more binding sites readily accessible, which is conducive to the effective capture of antibodies (Chen et al., 2019a). Taken all together, the PtCoCuPd HBTPs are chosen as the optimum material for constructing label-free immunosensors to improve the analytical performance.

3.4. Optimization of the experimental parameters for immunosensor

The experimental parameters closely determine the electroanalytical performance of the immunosensor, and thus the pH in the buffer, incubation time and the metal loading of PtCoCuPd HBTPs were critically optimized in this study (Zhang et al., 2019).

Fig. S1B (SI) shows the DPV plots of the PtPd NPs, PtCoPd NPs and PtCoCuPd HBTPs acquired in the PBS (0.1 moL L^{-1}) containing 5.0 mmol L^{-1} K_3 [Fe(CN)$_6$] at a pH range from 5.0 to 8.0. The peak current reaches the maximum at pH 7.4, due to the fact that neutral electrolyte is beneficial to maintain the activity and stability of antigen and antibody (Qian et al., 2019). Therefore, pH 7.4 is the optimal for the following experiments.

The incubation time significantly affects the specific binding between antigens and antibodies (Haji-Hashemi et al., 2018). As shown in Fig. S1C (SI), the peak currents descend sharply when the time is prolonged to 45 min, because the as-formed immune complexes between antigens and antibodies seriously hinder the charge transfer procedure. The peak currents tend to be constant by extending the time up to 60 min, illustrating the saturated binding between antigen and antibody (Gu et al., 2018). Therefore, 60 min is selected as the best in this context.

The loading of electrode materials reflects the intrinsic electrochemical characters in a label-free electrochemical immunosensor (Dai et al., 2019). The PtCoCuPd HBTPs with appropriate loading not only promote the binding of antigen and antibody, but also boost the catalytic activity (Lv et al., 2019). As displayed in Fig. S1D (SI), the peak currents increase gradually with the concentrations up to 1.5 mg mL^{-1}, followed by the adverse decrease in the electrochemical signals by loading excess PtCoCuPd HBTPs at 2.5 mg mL^{-1}, owing to the big increase in the interface mass transfer resistance (Wei et al., 2016). Hence, the optimum concentration of PtCoCuPd HBTPs is 1.5 mg mL^{-1}.

3.5. Detection of cTnI by this immunosensor

Under the optimal conditions, the prepared immunosensor is explored to detect cTnI using PtCoCuPd HBTPs to enhance the catalytic current of $K_3Fe(CN)_6$. As Fig. 5C illustrates, the peak currents of the probe linearly reduce with the increase of the cTnI concentrations, indicating the severe sluggish in the charge transfer because of the steric hindrance effects of the attached proteins. The currents display linear correlation with the logarithm of the cTnI concentrations within the scope of 0.001–100.0 ng mL^{-1}. The fitted linear regression equation is described as follows: $I = -55.74 \log C_{(cTnI)}$ (ng mL^{-1}) + 135.78, with the large correlation coefficient (R^2 = 0.985) and the *LOD* down to 0.2 pg mL^{-1} (S/N = 3, Fig. 5D).

As evidently illuminated in Table S1 (SI), the as-constructed immunosensor has the superior advantages (i.e. lower detection limits and broader linear range) for the detection of cTnI alternative to those reported previously such as multiwalled carbon nanotube-whiskered nanofibres (the linear range of 0.5–100 ng mL^{-1} and the *LOD* of 40 pg mL^{-1}) (Rezaei et al., 2018) and CdAgTe quantum dots (the linear range of 0.005–20 ng mL^{-1}; the *LOD* of 1.7 pg mL^{-1}) (Tan et al., 2017). Meanwhile, the as-developed immunosensor also has distinguished analytical properties relative to other non-electrochemical methods such as the functionalized Au NPs for colorimetric analysis of cTnI with the *LOD* of only 0.2 ng mL^{-1} (Liu et al., 2016).

3.6. Specificity, reproducibility and stability

Specificity is the main criterion for evaluating the performances of immunosensors (Fu et al., 2019). In this investigation, PSA, BSA, squmaous cell carcinoma antigen (SCCA) and carbohydrate antigen 125 (CA 125) served as interfering substances to seriously examine the specificity of the as-constructed immunosensor. In the specificity study, the peak currents of the probe at 0.1 ng mL^{-1} cTnI are almost identical in the absence and presence of each interfering substance (100.0 ng mL^{-1}). As Fig. 6A depicts, the relative standard deviation (*RSD*) is less than 4.8%, which manifests the good anti-interference property of the PtCoCuPd HBTPs-based immunosensor for cTnI detection.

Reproducibility is another factor in evaluating the immunosensor performance (Xie et al., 2015). Five immunosensors fabricated separately were adopted to detect cTnI (0.1 ng mL^{-1}) under the same operation conditions. As described in Fig. 6B, the electrochemical signals are nearly constant, and the *RSD* is calculated to be roughly 4.7%. It suggests the distinctively improved reproducibility of the as-built immunosensor.

Stability is another essential parameter of the immunosensor (Chen et al., 2017). The stability test was performed by storing the as-prepared immunosensor at 4 °C and detecting every seven days (Fig. 6C). There is no obvious change observed in the peak currents after the storage of 7 days in the refrigerator at 4 °C. The current still keeps 93.5% of its initial value after a longer period (e.g. 21 days), which shows the long-term stability of the as-obtained immunosensor.

3.7. Detection of cTnI in human serum

Accurate analysis of real samples is essential for practical applications of advanced immunosensors (Chen et al., 2019a). In order to exploit the practical applications of the constructed immunosensor, standard addition method was employed to detect cTnI in human serum. As seen from Table S2 (SI), the recoveries emerge in the range of 100.2%–100.6%, and the *RSD* is below 4.0%. These data manifest the acceptable accuracy. The strategy would have potential applications for the assay of other tumor markers in clinical diagnostics.

The outstanding analytical performances of the PtCoCuPd HBTPs-based immunosensor are mainly attributed to the inherent merits of the PtCoCuPd HBTPs: (i) PtCoCuPd HBTPs with spatially and locally separated branches provide abundant binding sites, thus facilitating the immobilization of the biomolecules and accelerating the electron transfer (Fu et al., 2016). (ii) The coexistence of four metals in the alloy offers a good biological microenvironment for immune recognition reaction (Barman et al., 2018). (iii) The incorporation of non-noble metals such as Co and Cu can greatly reduce the cost and improve the utility efficiency of Pt and Pd without deteriorating the catalytic activity (Liu et al., 2018). Concurrently, the synergistic effects between the four metals greatly improve the performance of the electroanalysis (Cao et al., 2013).

4. Conclusions

To sum up, unique PtCoCuPd HBTPs were prepared by a novel one-pot aqueous method. A label-free electrochemical immunosensor for the quantitative determination of cTnI was fabricated using PtCoCuPd HBTPs as signal amplification material. The as-synthesized PtCoCuPd HBTPs exhibited largely enhanced catalytic signals towards the probe, which were beneficial to the sequential assay of cTnI with the distinguished improvement in the sensitivity ($LOD = 0.2\ \mathrm{pg\ mL^{-1}}$) and linear range ($0.001–100.0\ \mathrm{ng\ mL^{-1}}$) under optimal conditions, along with the high specificity, acceptable reproducibility and long-term stability. The as-developed immunosensor can accurately detect cTnI in diluted serum samples, which would have potential applications for monitoring other tumor markers in early accurate diagnosis and in-situ monitoring of many cancers.

CRediT authorship contribution statement

Yao Chen: Investigation, Data curation, Formal analysis, Writing - original draft. **Li-Ping Mei:** Investigation, Data curation. **Jiu-Ju Feng:** Investigation, Conceptualization, Methodology, Supervision, Writing - review & editing. **Pei-Xin Yuan:** Investigation, Data curation. **Xiliang Luo:** Investigation, Data curation. **Ai-Jun Wang:** Conceptualization, Funding acquisition, Project administration, Supervision, Methodology, Writing - review & editing.

Declaration of competing interest

The authors declare that they have no known competing financial interests or personal relationships that could have appeared to influence the work reported in this paper.

Acknowledgements

This research was supported by National Natural Science Foundation of China (21475118, 21675093 and 21305124), Zhejiang Public Welfare Technology Application Research Project (LGG18E010001 and LGG19B050001), Natural Science Foundation of Zhejiang Province (Q19B050016), and Foundation of Key Laboratory of Sensor Analysis of Tumor Marker, Ministry of Education, Qingdao University of Science and Technology (SATM201703, STAM201804).

Appendix A. Supplementary data

Supplementary data to this article can be found online at https://doi.org/10.1016/j.bios.2019.111638.

References

Asif, M., Aziz, A., Ashraf, G., Wang, Z., Wang, J., Azeem, M., Chen, X., Xiao, F., Liu, H., 2018. ACS Appl. Mater. Interfaces 10, 36675–36685.
Barman, S.C., Hossain, M.F., Yoon, H., Park, J.Y., 2018. Biosens. Bioelectron. 100, 16–22.
Cao, X., Wang, N., Jia, S., Guo, L., Li, K., 2013. Biosens. Bioelectron. 39, 226–230.
Chen, X., Xu, W., Jiang, Y., Pan, G., Zhou, D., Zhu, J., Wang, H., Chen, C., Li, D., Song, H., 2017. Nanoscale 9, 16357–16364.
Chen, Y., Wang, A.-J., Yuan, P., Luo, X., Xue, Y., Feng, J.-J., 2019a. Biosens. Bioelectron. 132, 294–301.
Chen, Y., Yuan, P., Wang, A.-J., Luo, X., Xue, Y., Zhang, L., Feng, J.-J., 2019b. Biosens. Bioelectron. 126, 187–192.
Cho, I.-H., Paek, E.-H., Kim, Y.-K., Kim, J.-H., Paek, S.-H., 2009. Anal. Chim. Acta 632, 247–255.
Dai, L., Li, Y., Wang, Y., Luo, X., Wei, D., Feng, R., Yan, T., Ren, X., Du, B., Wei, Q., 2019. Biosens. Bioelectron. 132, 97–104.
Dhawan, S., Sadanandan, S., Haridas, V., Voelcker, N.H., Prieto-Simón, B., 2018. Biosens. Bioelectron. 99, 486–492.
Fu, S.-F., Zhu, C.-Z., Song, J.-H., Engelhard, M., Xia, H.-B., Du, D., Lin, Y.-H., 2016. ACS Appl. Mater. Interfaces 8, 22196–22200.
Fu, X., He, J., Zhang, C., Chen, J., Wen, Y., li, J., Mao, W., Zhong, H., Wu, J., Ji, X., Yu, C., 2019. Biosens. Bioelectron. 132, 302–309.
Gao, F., Zhou, F., Chen, S., Yao, Y., Wu, J., Yin, D., Geng, D., Wang, P., 2017. Analyst 142, 4308–4316.
Gao, Z.-Q., Li, Y.-Y., Zhang, C.-Y., Zhang, S., Li, F.-Y., Wang, P., Wang, H., Wei, Q., 2019. Biosens. Bioelectron. 126, 108–114.
Gu, X., She, Z., Ma, T., Tian, S., Kraatz, H.-B., 2018. Biosens. Bioelectron. 102, 610–616.
Haji-Hashemi, H., Habibi, M.M., Safarnejad, M.R., Norouzi, P., Ganjali, M.R., 2018. Sens. Actuators B Chem. 275, 61–68.
Liu, X., Wang, Y., Chen, P., McCadden, A., Palaniappan, A., Zhang, J., Liedberg, B., 2016. ACS Sens. 1, 1416–1422.
Liu, Z., Qi, J., Liu, M., Zhang, S., Fan, Q., Liu, H., Liu, K., Zheng, H., Yin, Y., Gao, C., 2018. Angew. Chem. Int. Ed. 130, 11852–11856.
Lv, H., Li, Y., Zhang, X., Li, X., Xu, Z., Chen, L., Li, D., Dong, Y., 2019. Biosens. Bioelectron. 133, 72–78.
Ma, H., Zhao, Y., Liu, Y., Zhang, Y., Wu, D., Li, H., Wei, Q., 2017. Anal. Chem. 89, 13049–13053.
Mao, W., He, J., Tang, Z., Zhang, C., Chen, J., Li, J., Yu, C., 2019. Biosens. Bioelectron. 131, 67–73.
Qi, T., Liao, J., Li, Y., Peng, J., Li, W., Chu, B., Li, H., Wei, Y., Qian, Z., 2014. Biosens. Bioelectron. 61, 245–250.
Qian, X., Zhou, X., Ran, X., Ni, H., Li, Z., Qu, Q., Li, J., Du, G., Yang, L., 2019. Biosens. Bioelectron. 130, 214–224.
Rezaei, B., Shoushtari, A.M., Rabiee, M., Uzun, L., Mak, W.C., Turner, A.P.F., 2018. Talanta 182, 178–186.
Seo, S.-M., Kim, S.-W., Park, J.-N., Cho, J.-H., Kim, H.-S., Paek, S.-H., 2016. Biosens. Bioelectron. 83, 19–26.
Shao, F.-Q., Feng, J.-J., Lin, X.-X., Jiang, L.-Y., Wang, A.-J., 2017. Appl. Catal. B Environ. 208, 128–134.
Shao, F.-Q., Lin, X.-X., Feng, J.-J., Yuan, J., Chen, J.-R., Wang, A.-J., 2016. Electrochim. Acta 219, 321–329.
Shi, Y.-C., Wang, A.-J., Yuan, P., Zhang, L., Luo, X., Feng, J.-J., 2018. Biosens. Bioelectron. 111, 47–51.
Spain, E., Carrara, S., Adamson, K., Ma, H., O'Kennedy, R., De Cola, L., Forster, R.J., 2018. ACS Omega 3, 17116–17124.
Tan, Y., Wang, Y., Li, M., Ye, X., Wu, T., Li, C., 2017. Biosens. Bioelectron. 91, 741–746.
Tian, L., Liu, L., Li, Y., Wei, Q., Cao, W., 2016. Sci. Rep. 6, 30849.
Wang, A.-J., Zhu, X.-Y., Chen, Y., Luo, X., Xue, Y., Feng, J.-J., 2019a. Sens. Actuators B Chem. 292, 164–170.
Wang, A.-J., Zhu, X.-Y., Chen, Y., Yuan, P.-X., Luo, X., Feng, J.-J., 2019b. Sens. Actuators B Chem. 288, 721–727.
Wang, H., Yin, S., Xu, Y., Li, X., Alshehri, A.A., Yamauchi, Y., Xue, H., Kaneti, Y.V., Wang, L., 2018. J. Mater. Chem. 6, 8662–8668.
Wei, Y., Li, Y., Li, N., Zhang, Y., Yan, T., Ma, H., Wei, Q., 2016. Biosens. Bioelectron. 79, 482–487.
Wen, W., Yan, X., Zhu, C., Du, D., Lin, Y., 2017. Anal. Chem. 89, 138–156.
Wu, D., Fan, H., Li, Y., Zhang, Y., Liang, H., Wei, Q., 2013. Biosens. Bioelectron. 46, 91–96.
Xie, S., Ye, J., Yuan, Y., Chai, Y., Yuan, R., 2015. Nanoscale 7, 18232–18238.
Yan, Q., Yang, Y., Tan, Z., Liu, Q., Liu, H., Wang, P., Chen, L., Zhang, D., Li, Y., Dong, Y., 2018. Biosens. Bioelectron. 103, 151–157.
Yang, Y.-Y., Liu, Q., Liu, Y., Cui, J.-J., Liu, H., Wang, P., Li, Y.-Y., Chen, L., Zhao, Z.-D., Dong, Y.-H., 2017. Biosens. Bioelectron. 90, 31–38.
Yang, Z.-H., Zhuo, Y., Yuan, R., Chai, Y.-Q., 2015. Biosens. Bioelectron. 69, 321–327.
Ye, J., Zhu, L., Yan, M., Zhu, Q., Lu, Q., Huang, J., Cui, H., Yang, X., 2019. Anal. Chem. 91, 1524–1531.
Zhang, X.-B., Li, Y., Lv, H., Feng, J., Gao, Z., Wang, P., Dong, Y., Liu, Q., Zhao, Z., 2018. Biosens. Bioelectron. 106, 142–148.
Zhang, X.-B., Lv, H., Li, Y., Zhang, C., Wang, P., Liu, Q., Ai, B., Xu, Z., Zhao, Z., 2019. J. Mater. Chem. B 7, 1460–1468.
Zhou, F., Yao, Y., Luo, J., Zhang, X., Zhang, Y., Yin, D., Gao, F., Wang, P., 2017. Anal. Chim. Acta 969, 8–17.
Zhu, C., Du, D., Eychmüller, A., Lin, Y., 2015. Chem. Rev. 115, 8896–8943.